

spEnhance: A Computational Framework for Trustworthy Super-Resolution Enhancement in Spatial Omics

Menghan Li^{1,2,†[0009–0007–3117–0570]}, Xutao Wang^{3,4,†[0009–0002–8167–595X]}, Su Xu^{3[0009–0003–3000–271X]}, Yuxin Yin^{3[0009–0005–5377–4928]}, Xingche Guo^{5,★[0000–0003–2001–9879]}, and Dongyuan Song^{3,★[0000–0003–1114–1215]}

¹ School of Life Sciences, Fudan University, Shanghai, China 200433

² Department of Neurosurgery, Stanford University School of Medicine, Stanford, CA 94305

³ Department of Genetics and Genome Sciences, University of Connecticut Health Center, Farmington, CT 06030

⁴ Division of Infectious Diseases, Center for Data Science, Rutgers University–New Jersey Medical School, Newark, NJ 07102

⁵ Department of Statistics, University of Connecticut, Storrs, CT 06269

†: These authors contributed equally to this work

★: To whom correspondence should be addressed. Email: dosong@uchc.edu; xingche.guo@uconn.edu

Abstract. The advent of spatial omics, especially spatial transcriptomics (ST), has enabled unprecedented insights into cellular heterogeneity and spatially regulated molecular programs. Within this spectrum of ST technologies, array-based platforms have become widely used for their transcriptome-wide coverage, but their spatial resolution remains limited. To overcome this barrier, numerous computational methods have been proposed to reconstruct high-resolution spatial gene expression from spot-level data by integrating histology; however, existing methods suffer from limited accuracy and reliability. Using only histological features, these methods are trained on a single dataset without a validation set, leading to overfitting and spurious gene expression patterns. Here we present spEnhance, a computational framework that reconstructs spatial gene expression with super-resolution from spot-level data while quantifying the confidence in its predictions. spEnhance achieves higher prediction accuracy by integrating both histology and single-cell RNA-seq (scRNA-seq) data, and employs a novel way to construct validation sets for trustworthy prediction. Beyond transcriptomics, spEnhance can also enhance other modalities, such as spatial alternative splicing and spatial chromatin accessibility. Comprehensive benchmarking across multiple tissues and platforms demonstrates that spEnhance achieves state-of-the-art accuracy, recovers fine-grained structure, and provides calibrated uncertainty estimates. Collectively, spEnhance establishes a generalizable and trustworthy framework for enhancing diverse spatial omics data, paving the way for more integrative and reliable analyses of spatial gene regulation.

Keywords: Spatial Omics · Spatial Transcriptomics · Histology · Truthworthy AI.

1 Introduction

Understanding the spatial organization of gene expression and regulation is essential to elucidate tissue architecture and cellular function [1]. Spatial omics technologies, including spatial transcriptomics [2], chromatin accessibility [3], and proteomics [4], now provide a means of characterizing transcriptional and regulatory landscapes *in situ*, advancing our understanding of spatial gene regulation.

Spatial transcriptomics (ST) technologies have evolved along two major directions. Imaging-based methods, such as MERFISH [5] and seqFISH [6], achieve subcellular resolution by multiplexed fluorescence imaging but are constrained by limited throughput and transcriptomic scope. In contrast, sequencing-based approaches (e.g., 10x Visium [7], Slide-seq [8], and Stereo-seq [9]) enable unbiased, transcriptome-wide profiling through spatially barcoded arrays, and uniquely retain full-length transcript information that supports analyses of alternative splicing and polyadenylation [10, 11]. Due to their lower cost, robustness, and scalability, sequencing-based ST platforms have been widely adopted, generating a large volume of publicly available datasets. However, their spatial resolution remains limited, as each capture spot aggregates transcripts from multiple cells, blurring fine-grained spatial organization. This trade-off between resolution and coverage has motivated the development of computational methods that enhance low-resolution ST data to achieve pixel-level resolution [12, 13, 14, 15, 16].

Despite recent progress, existing computational methods face several critical limitations. First, those methods are prone to overfitting due to the lack of validation data (the training and prediction are based on the same spatial slide), and they rarely provide quantitative assessments of prediction errors, limiting their trustworthiness. Second, most methods' enhancement relies solely on histological features, without leveraging other information such as single-cell transcriptome profiles or gene co-expression modules. Third, these methods are restricted to reconstructing spatial gene expression, whereas little effort has been made to extend enhancement to other modalities such as spatial alternative splicing or spatial chromatin accessibility.

To address these challenges, we present spEnhance, a trustworthy and generalizable computational framework for the super-resolution enhancement of spatial omics data. spEnhance integrates histological features, single-cell references, and gene co-expression modules to jointly predict spatial expression patterns while quantifying prediction errors. To mitigate overfitting, spEnhance innovatively employs a count-level data split strategy to construct independent training and validation sets. This unified architecture enables accurate and reliable enhancement of spatial gene expression and extends seamlessly to other omics modalities, including spatial alternative splicing and spatial chromatin accessibility. Comprehensive benchmarking across multiple tissues and platforms demonstrates that spEnhance achieves state-of-the-art accuracy and calibrated reliability, establishing a general framework for trustworthy spatial omics enhancement.

2 The spEnhance method

spEnhance (Fig. 1) reconstructs high-resolution spatial expression from spot-level spatial transcriptomics or other types of omics techniques by leveraging H&E-stained histology images and single-cell reference information. In the methods section, we use spatial transcriptomics as the primary illustrative example. More details are described in **Supplementary Materials**.

2.1 Histology feature extraction via dual-model embedding

To enable consistent analysis across whole-slide histological images acquired at varying resolutions, we first rescale each raw slide so that one pixel corresponds to a physical area of $0.5 \times 0.5 \mu\text{m}^2$. Under this calibration, a 16×16 pixel tile spans an $8 \times 8 \mu\text{m}^2$ region (approximately the size of a single cell). Suppose the histology image have height H and width W (in pixels). We then extract histological features via a dual-model strategy: (1) **HIPT** [17]: A hierarchical vision transformer that captures multi-scale tissue

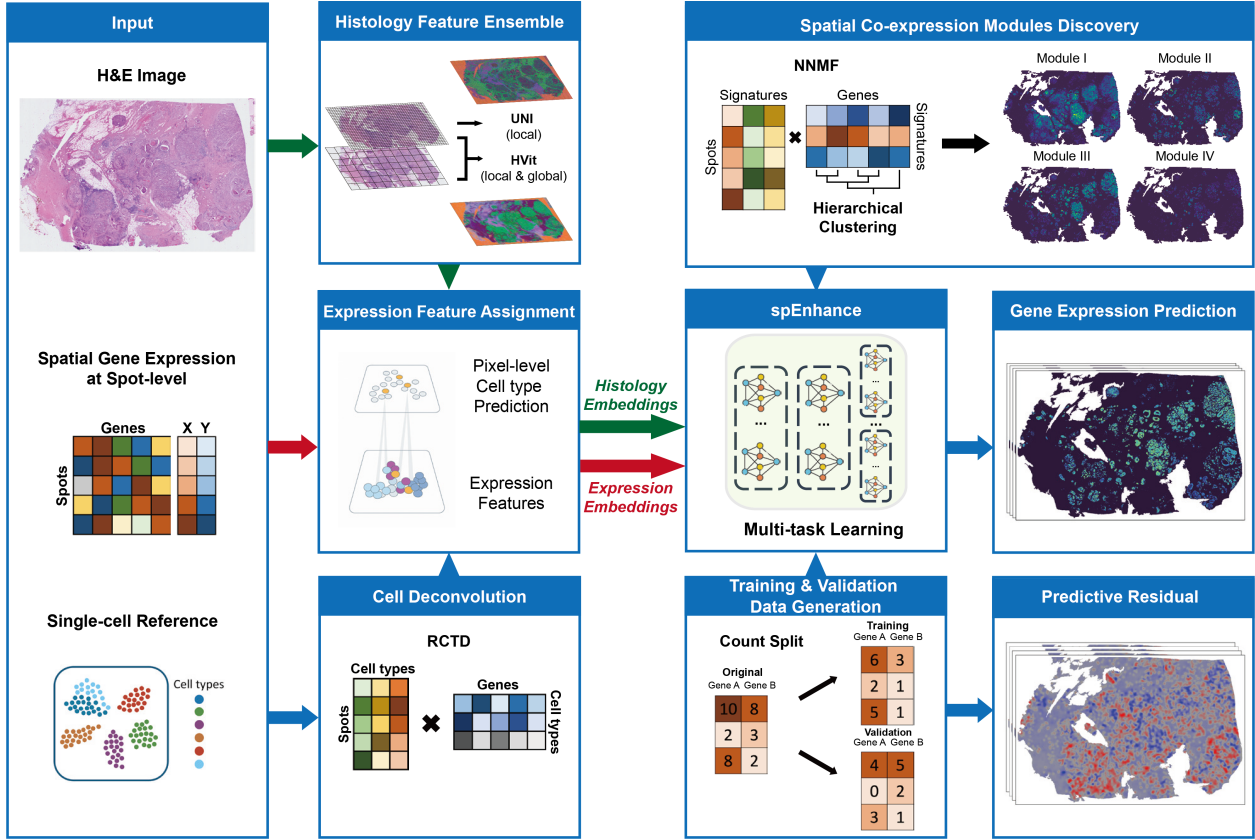


Fig. 1: Overview of the spEnhance workflow. spEnhance takes three types of inputs: the H&E image of a tissue section, its spot-level gene expression matrix, and an optional single-cell reference dataset (left). Histology features are extracted using two transformer-based models, and cell-type proportions are inferred via spot deconvolution to generate expression-derived features (middle). Spatial co-expression modules are identified and treated as separate prediction tasks, and a count split strategy produces independent training and validation data. Leveraging these histology and expression embeddings, spEnhance employs a multi-task learning framework to reconstruct high-resolution spatial gene expression profiles (right). The framework also outputs predictive residuals, which provide a quantitative measure of prediction reliability.

architecture. **(2) UNI** [18]: A universal pathology foundation model trained on over 100 million H&E tiles collected from diverse tissue types and disease contexts. Combining two complementary embeddings allows us combine global contextual representations (HIPT) with fine-grained local morphology (HIPT & UNI). A unified histology embedding is constructed by applying principal component analysis (PCA) to each model's features (retaining components that explain at least 99% of the variance) and then concatenating the reduced embeddings. Let $\mathbf{U} \in \mathbb{R}^{H_1 \times W_1 \times D}$ denote the histology embedding.

2.2 Single-cell reference guided gene expression embedding

A single-cell reference provides complementary molecular context beyond histology and can improve prediction. Below, we describe how we construct a gene-expression embedding from the single-cell reference.

Cell-type deconvolution using RCTD [19]: We built a single-cell reference by performing standard quality control and normalization, clustering cells, and manually curating cluster identities to obtain reliable cell-type labels. Next, we computed the cell type-by-gene reference matrix $\mathbf{R} \in \mathbb{R}^{C \times G}$, where each entry $R_{c,g}$ is the mean expression of gene g across all cells of type c . Using the Visium count matrix $\mathbf{Y} \in \mathbb{N}_0^{S \times G}$,

we then applied RCTD to deconvolve each spot, yielding $\mathbf{\Pi} = [\pi_{s,c}] \in [0, 1]^{S \times C}$, which estimates the fraction of each cell type present in spot $s = 1, \dots, S$ (rows summing to one).

Pixel-level cell type prediction: To predict pixel-level cell types, we train a graph convolutional network (GCN) [20] that maps the histology embedding \mathbf{U} to pixel-wise probabilities $\mathbf{P} \in [0, 1]^{H_1 \times W_1 \times C}$, using the spot-level deconvolution $\mathbf{\Pi}$ for weak supervision. In training, we first associate pixels with their corresponding spots. For pixel $v = (h, w)$, let $\hat{p}_v = (\hat{p}_{v,1}, \dots, \hat{p}_{v,C})$ denote the predicted cell-type probabilities. Averaging over pixels assigned to spot s yields $\hat{\pi}_{s,c} = |\mathcal{V}_s|^{-1} \sum_{v \in \mathcal{V}_s} \hat{p}_{v,c}$, where \mathcal{V}_s is the collection of pixels covered by spot s . We train the model by minimizing the Kullback–Leibler divergence from the spot-level target $\pi_s = (\pi_{s,1}, \dots, \pi_{s,C})$ to the aggregated prediction $\hat{\pi}_s$. For pixel-level evaluation, we partition the $H_1 \times W_1$ pixel grids into square regions, each of which covers the spatial extent of one spot. The partitioning was performed with a stride parameter k , such that adjacent regions overlapped by k rows or columns. Within each region, we apply the trained GCN to produce pixel-level predictions. For pixel v in overlapping regions, the final predicted probability vector was the average over all regions.

Gene expression feature assignment: Given the cell type-by gene reference matrix \mathbf{R} and the pixel-level cell-type probabilities \mathbf{P} , we assign a gene-expression value at pixel (h, w) via $V_{h,w,g}^{(0)} = \sum_{c=1}^C P_{h,w,c} R_{c,g}$. Collecting all genes and pixels forms the tensor $\mathbf{V}^{(0)} \in \mathbb{R}^{H_1 \times W_1 \times G}$. To extract compact representations, we reduce the gene dimension using truncated SVD to obtain the gene feature embedding $\mathbf{V} \in \mathbb{R}^{H_1 \times W_1 \times G_1}$.

2.3 Trustworthy prediction of super-resolution spatial gene expression

The predictive model: To predict pixel-level spatial gene expression $\mathbf{Z} \in \mathbb{R}^{H_1 \times W_1 \times G}$, we train a deep neural network that maps the fused histology–gene embeddings $\mathbf{F} = \text{Concat}(\mathbf{U}, \mathbf{V}) \in \mathbb{R}^{H_1 \times W_1 \times (D+G_1)}$ to \mathbf{Z} , using the spot-level count matrix \mathbf{Y} for weak supervision. Our model is a graph convolutional network (GCN) with two shared graph-convolution layers (512 hidden units each). To reflect the tendency of co-expressed genes to exhibit similar behavior, we adopt a **multi-task learning** design [21] in which genes are grouped into M spatial co-expression modules, identified via non-negative matrix factorization (NNMF [22]) on the count matrix \mathbf{Y} followed by hierarchical clustering. After the shared layers, each module is predicted by its own head (a linear layer mapping 512 to the number of genes in the module). A dropout layer ($p = 0.5$) is applied between the shared representation and each module-specific head to reduce overfitting.

Validation set construction: To address the common lack of replicates in spatial transcriptomics, where the entire spot-level dataset is often used for training without a hold-out set, we adopt a **count splitting** approach [23]: Given a spot-level count matrix $\mathbf{Y} = [Y_{s,g}] \in \mathbb{N}_0^{S \times G}$, we partition each entry as $Y_{s,g}^{(\text{train})} \sim \text{Binomial}(2Y_{s,g}, \frac{1}{2})$, $Y_{s,g}^{(\text{val})} = 2Y_{s,g} - Y_{s,g}^{(\text{train})}$. Under a Poisson model assumption, count splitting ensures that $Y_{s,g}^{(\text{train})}$ and $Y_{s,g}^{(\text{val})}$ follow the same distribution as $Y_{s,g}$, and are conditionally independent given their mean value. This construction therefore yields statistically independent training and validation sets suitable for unbiased assessment of predictive performance.

Trustworthy model training: For the training and validation set, we construct fused histology–gene embeddings $\mathbf{F}^{(\text{train})} = \text{Concat}(\mathbf{U}, \mathbf{V}^{(\text{train})})$ and $\mathbf{F}^{(\text{val})} = \text{Concat}(\mathbf{U}, \mathbf{V}^{(\text{val})})$, respectively. For training, pixel-level predictions are aggregated to the spot level via the predefined pixel–spot mapping \mathcal{V}_s . The network is fit by minimizing the square error loss between aggregated predictions and observed spot counts:

$$\mathcal{L}(\Theta) = \sum_{s=1}^S \sum_{m=1}^M \sum_{g \in \mathcal{G}_m} \left(Y_{s,g}^{(\text{train})} - \sum_{(h,w) \in \mathcal{V}_s} Z_{h,w,g}(\mathbf{F}^{(\text{train})}; \theta_m) \right)^2,$$

where $\Theta = \bigcup_{m=1}^M \theta_m$ collects the module-specific parameters and \mathcal{G}_m denotes the set of genes in module m . After each epoch, the validation loss is computed using $\mathbf{Y}^{(\text{val})}$ and $\mathbf{F}^{(\text{val})}$. The model checkpoint with the lowest validation loss is retained as the final trained model.

Model evaluation and predictive performance quantification: For pixel-level prediction, the trained model was applied to the complete (unsplit) embedding set \mathbf{F} , yielding the final super-resolution estimates of spatial gene expression. To quantify predictive performance, we first aggregate pixel-level predictions to the spot level and then compute spot-level predictive residuals between the observed and predicted spot-level counts. To stabilize the variance for count data, spEnhance uses square root transformation or Pearson residuals. This residual provides a convenient metric for assessing discrepancies between observed and predicted spot-level counts: positive values indicate underestimation, negative values indicate overestimation, and values near zero correspond to well-calibrated predictions.

3 Results

3.1 spEnhance outperforms existing methods across multiple semi-synthetic datasets

We systematically benchmarked spEnhance across diverse semi-synthetic ST datasets derived from human and mouse tissues, spanning multiple organs, pathological states, and measurement platforms (see **Supplementary Materials**). To obtain ground truth for quantitative evaluation, we used datasets generated by Xenium and Xenium Prime, which capture transcripts at subcellular resolution. Based on Visium spot size, spacing, and hexagonal layout, we aggregated Xenium /Xenium Prime pixel-level transcripts to generate pseudo-spot measurements. These pseudo-Visium matrices served as model inputs, and predictions were compared against the original pixel-level data to assess model performance.

According to gene-wise comparisons of structural similarity index measure (SSIM) [24] and Root Mean Square Error (RMSE), spEnhance demonstrated consistently superior performance compared with three state-of-the-art baselines: scstGCN [15], iStar [14], and TESLA [13], across all evaluated datasets (Fig. 2A). The performance advantage was substantial. For instance, on the human ovarian carcinoma dataset, spEnhance achieved a median SSIM of 0.9133 and a median RMSE of 0.050, markedly outperforming the competing models.

We also illustrate representative results using a human breast cancer dataset. Four biologically informative genes with distinct spatial architectures were selected: *ERBB2*, *ESR1*, *CD3E*, and *CTLA4*. For each gene, the pseudo-Visium input, Xenium Prime ground truth, and predictions from all competing methods were presented. Across all methods, spEnhance most accurately recapitulated both the spatial patterns and the expression scale of the ground truth, while other models frequently produced over-smoothed or distorted reconstructions (Fig. 2B). To further highlight differences in fine-grained spatial fidelity, we zoomed in on a small subregion in *ERBB2* predictions. In this higher-resolution view, spEnhance uniquely preserved sharp boundaries, local gradients, and focal expression hotspots that were either underestimated or blurred by other methods (Fig. 2C). This comparison demonstrates spEnhance’s ability to recover delicate tissue microstructures that are critical for downstream biological interpretation.

Finally, as spEnhance produces pixel-level predictions, they can be readily aggregated to single-cell resolution based on cell masks. We conducted refined nuclei segmentation using Cellpose-SAM [25] and obtained cell masks through nuclei expansion. We then aggregated pixel-level expression to cell-level based on the overlap between pixels and corresponding cells. The resulting single-cell-level expression maps reveal that spEnhance-derived estimates closely match the Xenium Prime ground truth with respect to both spatial distribution and cell-to-cell variability (Fig. 2D). This highlights the ability of spEnhance to generate biologically meaningful, cell-resolved reconstructions directly from spot-level inputs.

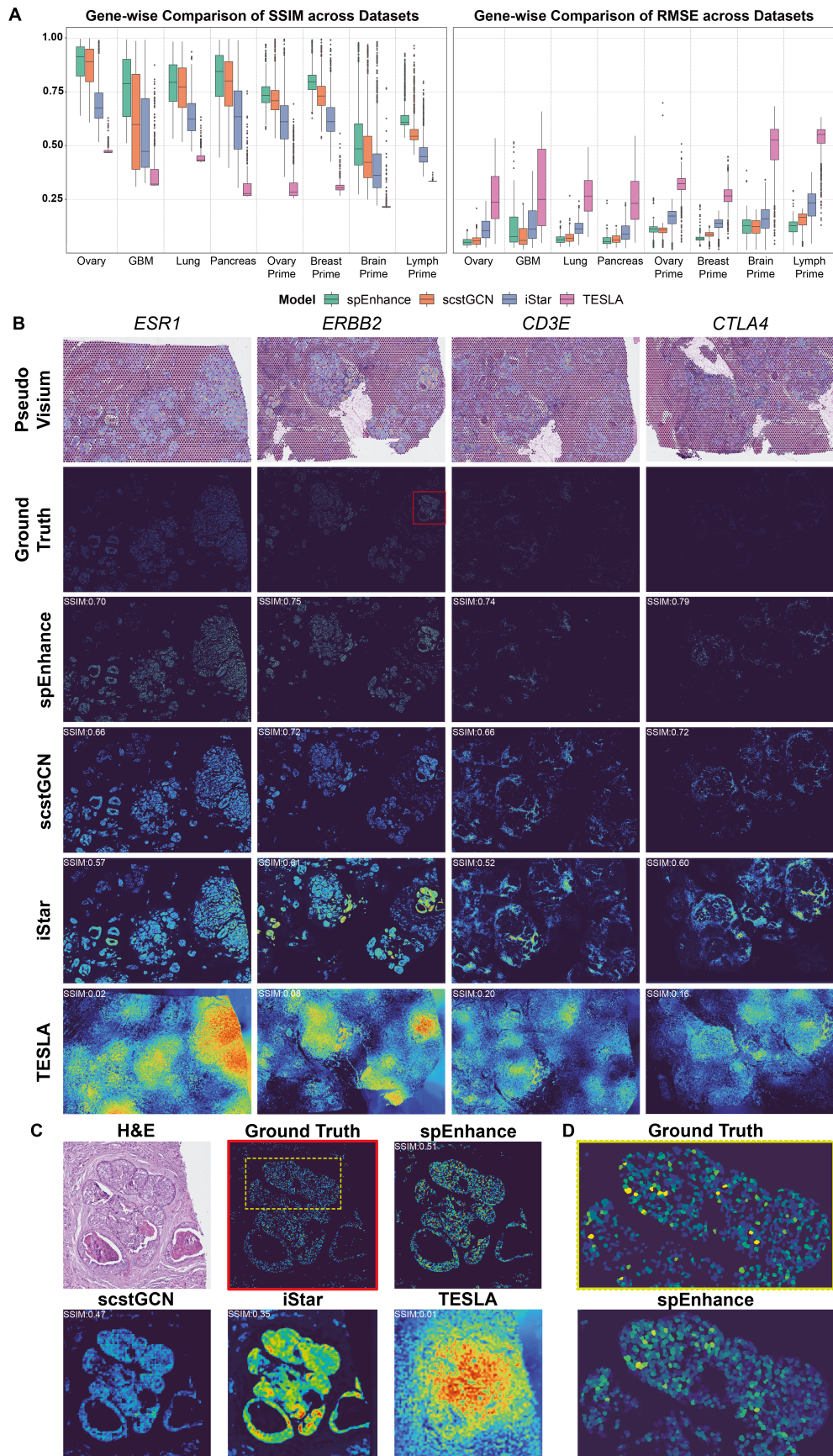


Fig. 2: Systematic evaluation of spEnhance prediction performance on multiple datasets. **(A)** Gene-wise comparison in terms of Structural Similarity Index Measure (SSIM, left) and Root Mean Square Error (RMSE, right) across all datasets against scstGCN, iStar, and TESLA. **(B)** Visualization of ground truth gene expression measured by Xenium Prime and predicted super-resolution gene expression by spEnhance, scstGCN, iStar, and TESLA. Each column represents a gene. The first two rows correspond to pseudo-Visium data and ground truth revealed by Xenium Prime, respectively. Subsequent rows represent prediction results by each model. **(C)** 8 \times enhancement was adopted to assist visualization a representative region. **(D)** Zoomed in view of a representative region. Histology feature, ground truth revealed by Xenium Prime and enhanced spatial gene expression by spEnhance of the same region were provided.

3.2 spEnhance avoids over-fitting and provides trustworthy error quantification

A major limitation of current ST enhancement approaches is the susceptibility of overfitting. Since models are trained and evaluated on a single tissue section, existing methods generally lack an appropriate validation strategy and therefore cannot reliably identify an optimal stopping point. In the context of ST prediction, the count splitting (CS) scheme provides a substantial advantage over the conventional random split. Under the spEnhance-CS framework, the validation loss reaches its minimum at approximately epoch 185 of 400 total training epochs, whereas the validation error under a random split continues to decline in parallel with the training loss, failing to exhibit a clear minimum (Fig. 3A; Fig. S1). We further provide a formal theoretical proof for the validity of such validation set construction in the **Supplementary Materials**.

To further illustrate the progression of model performance across training, we examined the imputed expression patterns of *IL6* at multiple epochs (Fig. 3B). The imputed signal is largely uninformative during the first 100 epochs, begins to emerge between epochs 150 and 250, and becomes distorted with continued training beyond this window. Notably, the highest structural similarity (SSIM = 0.69) within the examined subregion occurs at epoch 150, which is consistent with the validation-loss trajectory observed under the count-split strategy (Fig. 3A-B). This number is significantly smaller than the default settings in iStar [14] (400) and scstGCN [15] (500).

When examining individual genes, the Spearman rank correlation (SRCC) between the predictive residuals from spEnhance-CS and the true test error is consistently high across four representative genes (Fig. 3C), demonstrating that the residuals provide reliable spatial error quantification. To assess whether spEnhance-CS also reflects variation in prediction quality across genes, we further compared gene-wise performance metrics on the validation set with those on the test set. The strong linear relationship observed between these two sets of metrics (Fig. 3D) indicates that the validation set accurately captures cross-gene differences in prediction accuracy. Together, these results show that the spEnhance-CS validation set and predictive residuals substantially enhance the trustworthiness of spatial gene expression enhancement.

3.3 spEnhance enables more accurate tissue segmentation from enhanced spatial data

To evaluate whether super-resolved profiles enable more biologically informative downstream analyses, we performed unsupervised tissue segmentation on spEnhance-enhanced data across diverse tissues and platforms using BANKSY [26]. In a Xenium human breast cancer dataset, segmentation based on spEnhance predictions accurately recovered major pathological compartments, clearly distinguishing invasive carcinoma from ductal carcinoma *in situ* (DCIS). Moreover, spEnhance resolved transcriptional differences between DCIS-1 and DCIS-2, yielding clusters that closely matched expert annotations, while scstGCN failed to separate the two DCIS subregions (Fig. 4A). In addition, the preliminary cell-type maps generated by spEnhance already delineated invasive and DCIS compartments with reasonable accuracy, providing an auxiliary and interpretable layer of biological context.

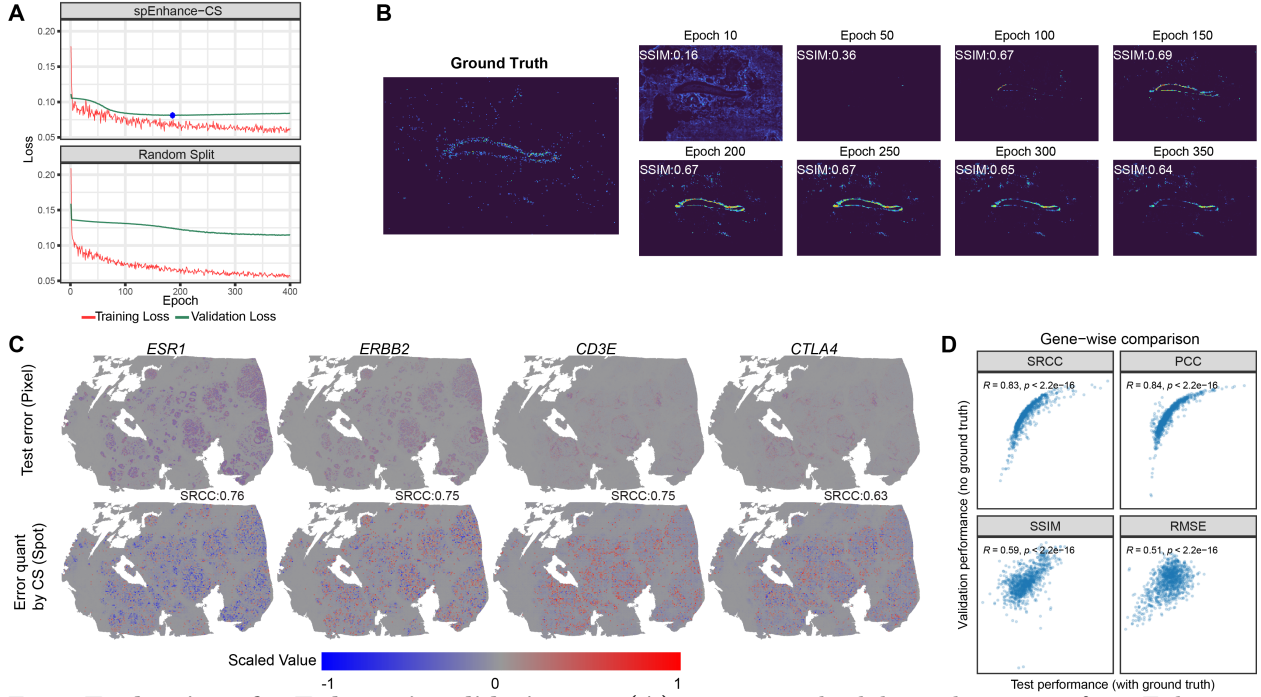


Fig. 3: Evaluation of spEnhance’s validation set. **(A)** Training and validation loss curves for spEnhance–Count Split (spEnhance-CS) and a random split. The blue star marks the epoch with the minimum validation loss. **(B)** Ground-truth gene expression (left) and predicted super-resolution gene expression across training epochs (right). The Structural Similarity Index Measure (SSIM) quantifies the agreement between predictions and ground truth. **(C)** Comparison between spEnhance-CS error quantification (no ground truth) and the true test error (with ground truth) for four representative genes. The Spearman Rank Correlation Coefficient (SRCC) measures the correspondence between the estimated and actual spatial prediction errors. **(D)** Gene-wise comparison of validation performance (four metrics) based on spEnhance-CS (no ground truth) versus test performance (with ground truth). The Pearson correlation R and corresponding p -values summarize the concordance between validation-based and true performance across genes.

Applying the same workflow to a Xenium human gastric cancer dataset [27], we found that segmentation derived from spEnhance-reconstructed profiles aligned closely with pathologist-defined regions and successfully highlighted key structures, including lymphoid aggregates and cohesive carcinoma regions (Fig. 4B). Notably, spEnhance also improved the identification of tertiary lymphoid structures (TLS), yielding substantially fewer false-positive TLS calls compared with the newly published approach iSCALE [27] (35.9% vs. 17.9%; Fig. 4C), demonstrating enhanced specificity for immune-rich microenvironments.

We further benchmarked segmentation quality in a Xenium Prime healthy mouse brain dataset by generating pseudo-Visium inputs and comparing segmentations obtained from Xenium ground truth, spEnhance predictions, and scstGCN predictions. spEnhance achieved a higher Adjusted Rand Index (ARI) relative to ground truth (0.110 vs. 0.085), indicating improved reconstruction of canonical spatial domains (Fig. 4D). Regionally, spEnhance-based segmentation more faithfully recapitulated neuroanatomical boundaries, particularly within the hippocampal formation (HPF), and showed closer agreement with structures annotated in the Allen Brain Atlas [28] than scstGCN.

Taken together, these cross-tissue analyses demonstrate that spEnhance generates super-resolved spatial profiles that substantially improve the accuracy and biological interpretability of downstream tissue segmentation across both pathological and normal tissues.

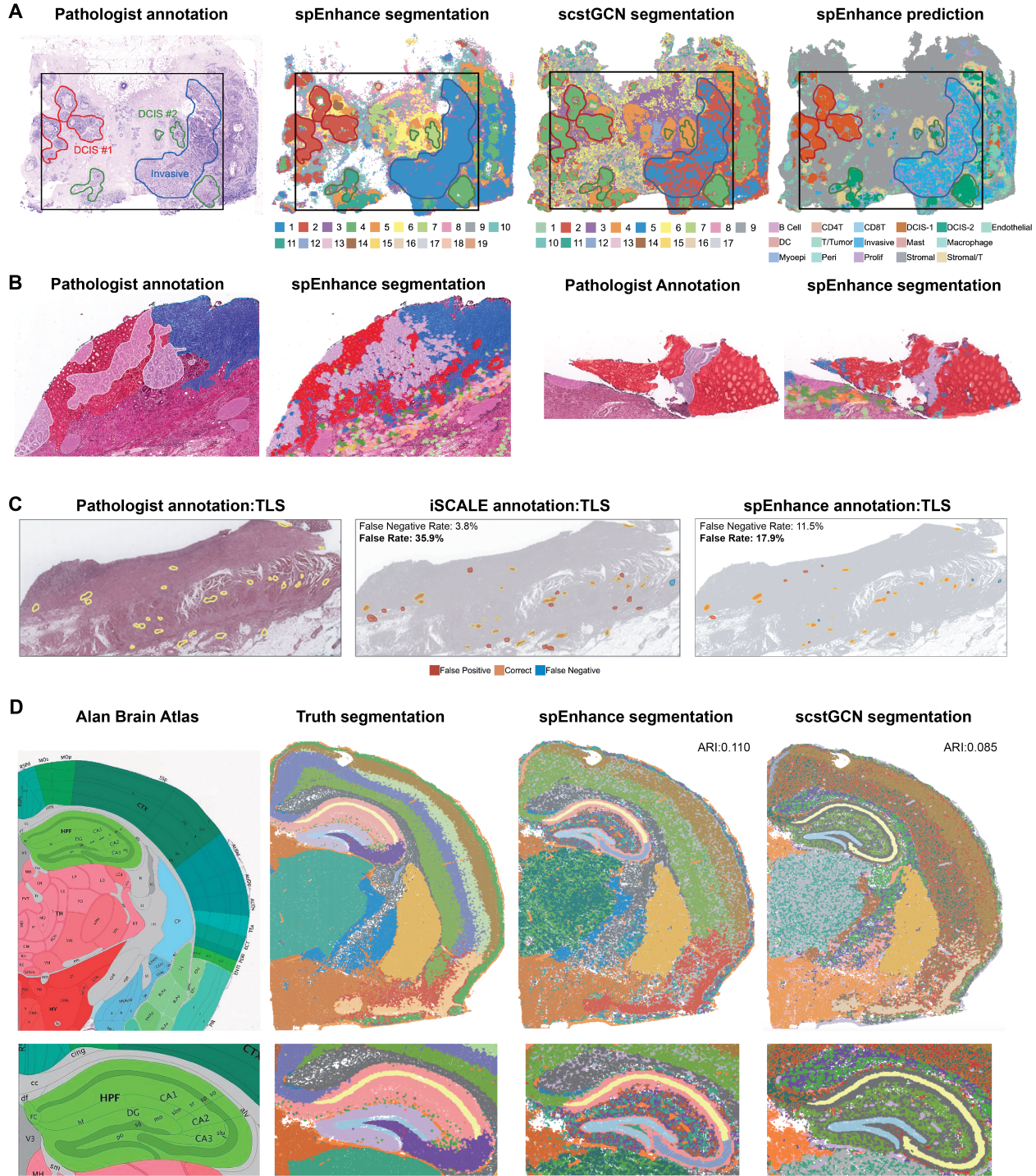


Fig. 4: Evaluation of spEnhance segmentation performance. (A) Comparison of unsupervised tissue segmentation by spEnhance and scstGCN with pathologist annotation of a human breast cancer data. The model was trained using Visium data mapped to the Xenium captured H&E image. (B) Tissue segmentation of gastric cancer data using spEnhance. Poorly cohesive carcinoma, blue; lymphoid aggregate, pink; normal gastric mucosal gland, red; intestinal metaplasia, purple. (C) Benchmarking TLS detection using spEnhance against iScale. Pathologist annotation is cited from iSCALE and treated as the ground truth. (D) Comparison of brain tissue segmentation using spEnhance and scstGCN. Models were trained using pseudo-visium data from pixel-level gene expression captured by Xenium Prime platform. Tissue segmentation using Xenium Prime data was treated as truth segmentation. Adjusted Rand Index (ARI) labels the concordance of clusters between truth segmentation and segmentation from spEnhance and scstGCN.

3.4 spEnhance supports multiple modal spatial enhancement

Owing to the shared measurement principles and data structures among array-based spatial omics technologies, spEnhance can be readily generalized beyond spatial transcriptomics to modalities such as spatial chromatin accessibility and spatial alternative splicing (AS).

We evaluated this capability using a human glioblastoma (GBM) dataset profiled on the Visium platform [29], for which matched short-read and long-read sequencing were generated from the same section. spEnhance was applied to short-read-based gene expression to obtain pixel-level super-resolved maps, and independently to long-read-based isoform expression to reconstruct pixel-level isoform abundance.

To assess the biological insights enabled by enhanced resolution, we first computed module scores for Hypoxic, Tumor, Invasive, and Vascular programs using established gene signatures and assigned each Visium spot to its highest-scoring module, generating a baseline spot-level segmentation (Fig. 5A). Applying spEnhance followed by unsupervised clustering on reconstructed pixel-level gene expression yielded eight spatially coherent clusters (Fig. 5A). Clusters 6 and 8 corresponded closely to the hypoxic niche defined from spot-level segmentation, but spEnhance further subdivided this compartment, revealing a distinct subregion represented by cluster 8. Differential expression analysis identified marked transcriptional differences between clusters 8 and 6: genes such as *SOD2* and *JUN* were strongly upregulated in cluster 8 (Fig. 5B), and pathway enrichment indicated preferential activation of hypoxia-related programs—including HIF-1 signaling and glycolysis—as well as ribosome and protein-synthesis pathways (Fig. 5D). Notably, *TIMP1* exhibited substantially higher expression in cluster 8, and survival analysis based on TCGA data associated high *TIMP1* expression with poor prognosis in GBM patients (Fig. 5C), suggesting that this subregion represents a clinically relevant hypoxic microenvironment. Isoform-level analysis further revealed distinct isoform usage within the hypoxic niche: while *TIMP1-202* was rarely expressed, *TIMP1-204* and *TIMP1-201* were specifically enriched in cluster 8 (Fig. 5E), highlighting the additional biological resolution gained from isoform-resolved spatial reconstruction.

We further extended spEnhance to spatial chromatin accessibility using a human cerebellum spatial ATAC-seq dataset [30]. After peak calling and constructing a spot×peak accessibility matrix, we applied spEnhance to generate pixel-level chromatin accessibility maps. The predicted total fragment counts showed strong correspondence with underlying anatomical structures (Fig. 5F). Clustering based on the enhanced maps produced tissue segmentation closely aligned with known cerebellar anatomy while revealing finer subregional distinctions not captured by the original annotation (Fig. 5F). These results demonstrate that spEnhance robustly enhances spatial epigenomic data and enables recovery of high-resolution chromatin accessibility landscapes that faithfully reflect biological tissue architecture.

4 Discussion

In conclusion, spEnhance provides accurate and trustworthy enhancement of spatial omics data, including spatial transcriptomics, spatial ATAC-seq and spatial isoform quantification. Our results show that spEnhance substantially outperforms existing methods in reconstructing high-resolution gene expression and in multiple downstream analyses. To the best of our knowledge, spEnhance is the first framework to introduce a validation set for the single-slice enhancement problem. The validation set generated through count split reliably predicts test error and effectively mitigates overfitting. While the current spEnhance Count Split is based on the Poisson distribution assumption, a more generalizable data thinning approach can be applied for other distributions, for example, Negative Binomial distribution [32]. spEnhance integrates several previously published computational components, the framework itself is fully modular: key steps, including histology feature extraction, spot deconvolution, co-expression module identification, and the loss function,

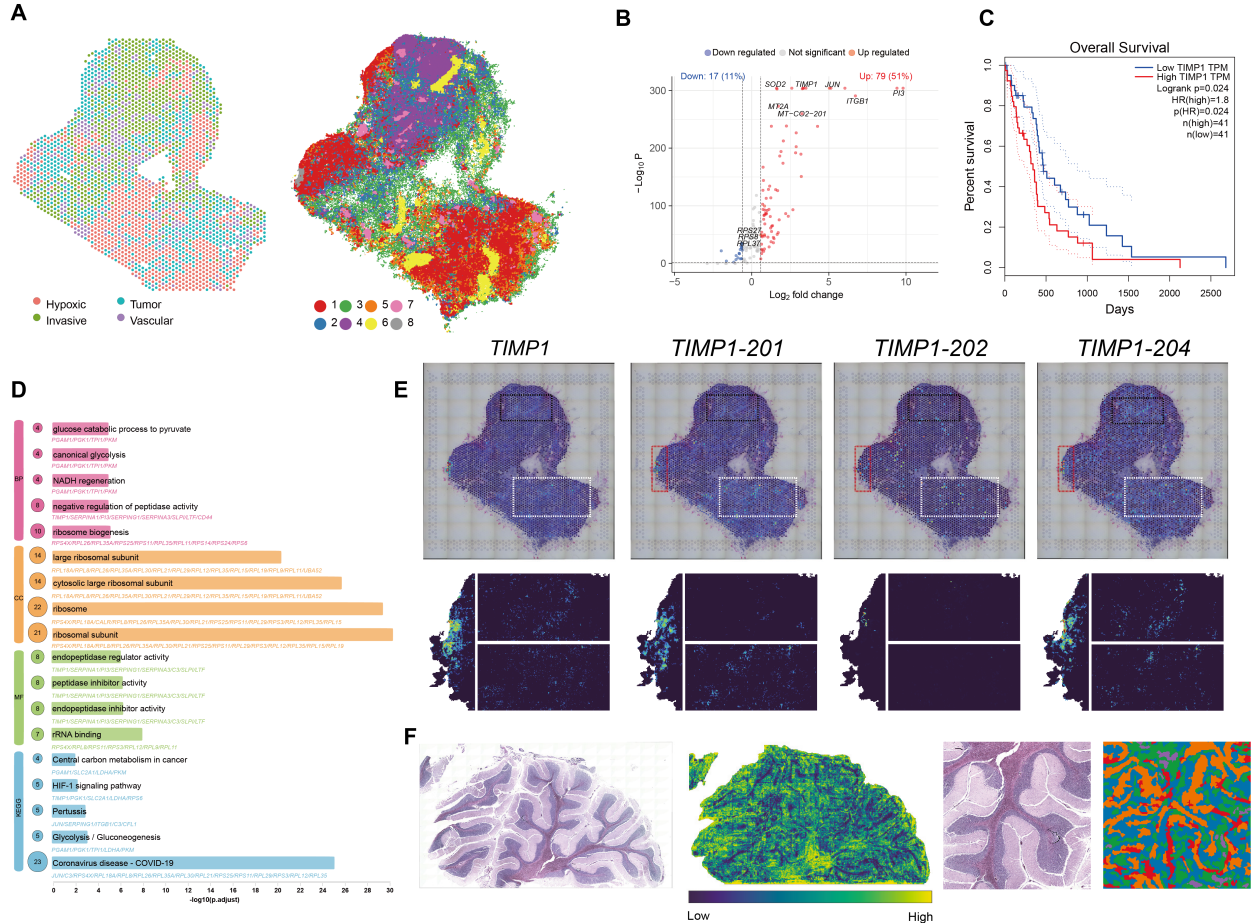


Fig. 5: Extension of spEnhance to spatial ATAC-seq and spatial alternative splicing analysis.

(A) Tissue segmentation based on spot-level data and spEnhance reconstructed pixel-level data. Spot-level module scores for 4 expression programs (Hypoxic, Tumor, Invasive and Vascular) was calculated as described in [29]. Spot was assigned to the module with highest scores. BANKSY was adopted for segmentation using spEnhance predictions [26]. **(B)** Volcano plot indicating differentially expression genes in cluster 8 against cluster 6. **(C)** Survival curve for GBM patients with high or low *TIMP1* expression in TCGA dataset. Survival analysis was conducted using GEPIA [31]. **(D)** Barplot showing top up-regulated pathways enriched in cluster 8 against cluster 6. BP, biological process;CC, cellular component; MF, molecular function. **(E)** Spot-level- and spEnhance reconstructed pixel-level-expression of *TIMP1* and corresponding isoforms detected. Representative subregions for spEnhance predictions were shown. **(F)** Spatial chromatin accessibility enhancement and subregion delineation in human cerebellum. Left to right: HE image of the cerebellar tissue section; spatial map of the total number of ATAC fragments predicted per pixel; zoomed-in HE image highlighting cerebellar subregions; tissue segmentation derived from spEnhance-enhanced pixel-level chromatin accessibility profiles.

can be readily replaced or upgraded as newer and more powerful methods become available. In the next step, we will further improve the model for other spatial omics features (e.g., spatial histone modification) and the joint prediction of spatial multi-omics (e.g., transcriptomics + ATAC).

Code Availability

The Python package spEnhance is available at <https://github.com/dsong-lab/spEnhance>.

Funding

This work was supported by the following grants: UConn Health faculty start-up (to D.S.).

References

- [1] Cameron G Williams et al. “An introduction to spatial transcriptomics for biomedical research”. In: *Genome medicine* 14.1 (2022), p. 68.
- [2] Lambda Moses and Lior Pachter. “Museum of spatial transcriptomics”. In: *Nature methods* 19.5 (2022), pp. 534–546.
- [3] Yanxiang Deng et al. “Spatial profiling of chromatin accessibility in mouse and human tissues”. In: *Nature* 609.7926 (2022), pp. 375–383.
- [4] Emma Lundberg and Georg HH Borner. “Spatial proteomics: a powerful discovery tool for cell biology”. In: *Nature Reviews Molecular Cell Biology* 20.5 (2019), pp. 285–302.
- [5] Jeffrey R Moffitt et al. “Molecular, spatial, and functional single-cell profiling of the hypothalamic preoptic region”. In: *Science* 362.6416 (2018), eaau5324.
- [6] Kok Hao Chen et al. “Spatially resolved, highly multiplexed RNA profiling in single cells”. In: *Science* 348.6233 (2015), aaa6090.
- [7] 10x Genomics. *Inside Visium Spatial Capture Technology*. https://pages.10xgenomics.com/rs/446-PB0-704/images/10x_BR060_Inside_Visium_Spatial_Technology.pdf. Accessed: 2025-09-04. 2019.
- [8] Samuel G Rodrigues et al. “Slide-seq: A scalable technology for measuring genome-wide expression at high spatial resolution”. In: *Science* 363.6434 (2019), pp. 1463–1467.
- [9] Ao Chen et al. “Spatiotemporal transcriptomic atlas of mouse organogenesis using DNA nanoball-patterned arrays”. In: *Cell* 185.10 (2022), pp. 1777–1792.
- [10] Natan Belchikov et al. “Understanding isoform expression by pairing long-read sequencing with single-cell and spatial transcriptomics”. In: *Genome Research* 34.11 (2024), pp. 1735–1746.
- [11] Jiayu Su et al. “A computational framework for mapping isoform landscape and regulatory mechanisms from spatial transcriptomics data”. In: *bioRxiv* (2025), pp. 2025–05.
- [12] Ludvig Bergenstråhlé et al. “Super-resolved spatial transcriptomics by deep data fusion”. In: *Nature biotechnology* 40.4 (2022), pp. 476–479.
- [13] Jian Hu et al. “Deciphering tumor ecosystems at super resolution from spatial transcriptomics with TESLA”. In: *Cell systems* 14.5 (2023), pp. 404–417.
- [14] Daiwei Zhang et al. “Inferring super-resolution tissue architecture by integrating spatial transcriptomics with histology”. In: *Nature biotechnology* 42.9 (2024), pp. 1372–1377.
- [15] Shuailin Xue et al. “Inferring single-cell resolution spatial gene expression via fusing spot-based spatial transcriptomics, location, and histology using GCN”. In: *Briefings in Bioinformatics* 26.1 (2024).
- [16] Jeongbin Park et al. “Generation of super-resolution images from barcode-based spatial transcriptomics by deep image prior”. In: *Cell Reports Methods* 5.1 (2025).
- [17] Richard J Chen et al. “Scaling vision transformers to gigapixel images via hierarchical self-supervised learning”. In: *Proceedings of the IEEE/CVF conference on computer vision and pattern recognition*. 2022, pp. 16144–16155.
- [18] Richard J Chen et al. “Towards a general-purpose foundation model for computational pathology”. In: *Nature medicine* 30.3 (2024), pp. 850–862.
- [19] Dylan M Cable et al. “Robust decomposition of cell type mixtures in spatial transcriptomics”. In: *Nature biotechnology* 40.4 (2022), pp. 517–526.
- [20] Thomas N. Kipf and Max Welling. “Semi-Supervised Classification with Graph Convolutional Networks”. In: *International Conference on Learning Representations*. 2017. URL: <https://openreview.net/forum?id=SJU4ayYgl>.

- [21] Sebastian Ruder. “An overview of multi-task learning in deep neural networks”. In: *arXiv preprint arXiv:1706.05098* (2017).
- [22] Ragnhild Laursen et al. “Neighborhood nonnegative matrix factorization identifies patterns and spatially-variable genes in large-scale spatial transcriptomics data”. In: (2025).
- [23] Ameer Dharamshi et al. “Generalized data thinning using sufficient statistics”. In: *Journal of the American Statistical Association* 120.549 (2025), pp. 511–523.
- [24] Zhou Wang et al. “Image quality assessment: from error visibility to structural similarity”. In: *IEEE transactions on image processing* 13.4 (2004), pp. 600–612.
- [25] Marius Pachitariu, Michael Rariden, and Carsen Stringer. “Cellpose-SAM: superhuman generalization for cellular segmentation”. In: *bioRxiv* (2025), pp. 2025–04.
- [26] Vipul Singhal et al. “BANKSY unifies cell typing and tissue domain segmentation for scalable spatial omics data analysis”. In: *Nature genetics* 56.3 (2024), pp. 431–441.
- [27] Anne Schroeder et al. “Scaling up spatial transcriptomics for large-sized tissues: uncovering cellular-level tissue architecture beyond conventional platforms with iSCALE”. In: *Nature Methods* (2025), pp. 1911–1922.
- [28] Quanxin Wang et al. “The Allen mouse brain common coordinate framework: a 3D reference atlas”. In: *Cell* 181.4 (2020), pp. 936–953.
- [29] Yanming Ren and et al. “Spatial transcriptomics reveals niche-specific enrichment and vulnerabilities of radial glial stem-like cells in malignant gliomas”. In: *Nature Communications* 14.1 (2023), p. 1028.
- [30] P. Guo et al. “Spatial profiling of chromatin accessibility in formalin-fixed paraffin-embedded tissues”. In: *Nature Communications* 16 (2025), p. 5945.
- [31] Zefang Tang and et al. “GEPIA: a web server for cancer and normal gene expression profiling and interactive analyses”. In: *Nucleic Acids Research* 45.W1 (2017), W98–W102.
- [32] Anna Neufeld et al. “Data thinning for convolution-closed distributions”. In: *Journal of Machine Learning Research* 25.57 (2024), pp. 1–35.